1   Continental pollution in the Western Mediterranean basin: large variability of

2   the aerosol single scattering albedo and influence on the direct shortwave

3   radiative effect

4   C. Di Biagio[1], P. Formenti[1], L. Doppler[2], C. Gaimoz[1], N. Grand[1], G. Ancellet[3], J.-L. Attié[4,5],

5   S. Bucci[6,7], P. Dubuisson[8], F. Fierli[6], M. Mallet[9], and F. Ravetta[3]

6   *[1] LISA, UMR CNRS 7583, Université Paris Est Créteil et Université Paris Diderot, Institut Pierre*
7   *Simon Laplace, Créteil, France*

8   *[2] Deutscher Wetterdienst, Metorological Observatory Lindenberg, Germany*

9   *[3] Sorbonne Universités, UPMC Univ. Paris 06; Université Versailles St-Quentin; CNRS/INSU,*
10   *LATMOS-IPSL, Paris, France*

11   *[4] Laboratoire d'Aérologie, University of Toulouse, UMR 5560 CNRS, France*

12   *[5] CNRM GAME UMR 3589 CNRS, METEO-FRANCE*

13   *[6] Institute for Atmospheric Sciences and Climate of the National Research Council , (ISAC-CNR),*
14   *Rome, 00133, Italy*

15   *[7] Sc. Dept. of Physics, Ferrara University, Ferrara, 44121, Italy*

16   *[8] Laboratoire d'Optique Atmosphérique, Université Lille 1, Villeneuve d'Ascq, France*

17   *[9] Laboratoire d'Aérologie, Observatoire Midi-Pyrénées, 14 Avenue Edouard Belin, 31400 Toulouse,*
18   *France*

20   Corresponidng author:

21   Claudia Di Biagio, claudia.dibiagio@lisa.u-pec.fr

34   **Abstract**

35   Pollution aerosols strongly influence the composition of the Western Mediterranean basin,

36   but at present little is known on their optical properties. We report in this study in situ

37   observations of the single scattering albedo (ω) of pollution aerosol plumes measured over

38   the Western Mediterranean basin during the TRAQA (TRansport and Air QuAlity) airborne

39   campaign in summer 2012. Cases of pollution export from different source regions around

40   the basin and at different altitudes between ~160 and 3500 m above sea level have been

41   sampled during the flights. Data from this study show a large variability of ω, with values

42   between 0.84-0.98 at 370 nm and 0.70-0.99 at 950 nm. The single scattering albedo generally

43   decreases with the wavelength, with some exception associated to the mixing of pollution

44   with sea spray over the sea surface. Lowest values of ω (0.84-0.70 between 370 and 950 nm)

45   are measured in correspondence of a fresh plume possibly linked to ship emissions over the

46   basin. The range of variability of ω observed in this study seems to be independent of the

47   source region around the basin, as well as of the altitude and ageing time of the plumes. The

48   observed variability of ω reflects in a large variability for the complex refractive index of

49   pollution aerosols, which is estimated to span in the large range 1.41-1.75 and 0.002-0.068

50   for the real and the imaginary parts, respectively, between 370 and 950 nm.

51   Radiative calculations in clear-sky conditions have been performed with the GAME radiative

52   transfer model to test the sensitivity of the aerosol shortwave Direct Radiative Effect (DRE)

53   to the variability of ω as observed in this study. Results from the calculations suggest up to a

54   50% and 30% change of the forcing efficiency (FE), i.e. the DRE per unit of optical depth, at

55   the surface ($-160 \div -235$ $Wm^{-2}\tau^{-1}$ at 60° solar zenith angle) and at the Top-Of-Atmosphere ($-

56   137 \div -92$ $Wm^{-2}\tau^{-1}$) for ω varying between its maximum and minimum value. This induces a

57   change of up to an order of magnitude ($+23 \div +143$ $Wm^{-2}\tau^{-1}$) for the radiative effect within the

58   atmosphere.

59

60

61   **Keywords**: pollution aerosols, single scattering albedo, direct radiative effect, Western

62   Mediterranean

63

64

65

1. Introduction

Atmospheric aerosols play a crucial role on climate by affecting the radiative transfer of atmospheric radiation and by modifying cloud properties and lifetime (Boucher et al., 2013). The capability of atmospheric aerosols to interact through processes of scattering and absorption with the atmospheric radiation, so to exert a direct radiative effect (DRE), depends on their spectral optical properties (extinction efficiency, k_{ext}, single scattering albedo, ω, and asymmetry factor, g). In particular the single scattering albedo has been demonstrated to be a key parameter in modulating the surface, Top-of-Atmosphere (TOA), and atmospheric aerosol DRE (e.g., Ramana and Ramanathan, 2006; Di Biagio et al., 2010; Loeb and Su, 2010). Aerosol optical properties can largely vary depending on the particles composition, size distribution, and shape, which are function of the aerosol source, type, and processing occurring during atmospheric lifetime. At present, the capability of climate models in reproducing all the possible heterogeneity in aerosol optical properties represents one the main source of uncertainty in evaluating their DRE on climate (McComiskey et al., 2008; Stier et al., 2013). In this sense, intensive studies providing with the characterization of the aerosol optical properties and their local and regional variability are of great importance in order to reduce these uncertainties.

This is particularly the case of the Western Mediterranean basin. Indeed, the Mediterranean is a very complex region, characterized by the presence of air masses carrying aerosols of different origins and types (Gkikas et al., 2012). On its northern bound, it is limited by Europe, which makes that anthropogenic pollution is usually exported from the continent towards the basin (Lelieveld et al., 2002; Pace et al., 2006). In particular, the Western part of the Mediterranean basin, surrounded by large coastal megacities, commercial harbours, and under the direct influence of some of the most industrialized areas of the continent (such as the Po Valley in Northern Italy or the Fos/Berre area in Southern France), is strongly affected by continental pollution outflows (Pérez et al., 2008; Pey et al., 2010; Di Biagio et al., 2015). The build-up of high pollution levels over the Western basin is particularly favoured during summer when the strong insolation enhances photochemical reactions and the stable meteorological conditions promote the stagnation of pollutants (Millan et al., 2000; Mallet et al., 2005).

In spite of this, the characterization of the optical properties of anthropogenic aerosols in this part of the basin remains only limited to coastal and inland regions (Mallet et al., 2003, 2011, 2013; Lyamani et al., 2006; Estelles et al., 2007; Saha et al., 2008; Esteve et al., 2012;

99   Piazzola et al., 2012; Pandolfi et al., 2011 and 2014), or remote islands actually far from the

100 strong influence of continental outflows (Lyamani et al., 2015). Moreover, the majority of

101 these studies uses remote sensing measurements and analyse aerosol properties integrated

102 over the entire atmospheric column, without information on their vertical variability. Thus, at

103 present, we miss a detailed characterization of the optical properties of the pollution aerosol

104 over the entire region, in particular over the remote sea, and its vertical distribution.

105 To fill this gap, the international ChArMEx (Chemistry-Aerosol Mediterranean Experiment;

106 http://charmex.lsce.ipsl.fr) research program has supported in recent years two airborne

107 campaigns over the Western Mediterranean basin: TRAQA (Transport and Air QuAlity) in

108 2012 and SAFMED (Secondary Aerosol Formation in the MEDiterranean) in 2013.

109 In a recent paper, Di Biagio et al. (2015) have presented in situ measurements of the aerosol

110 vertical profiles acquired over the remote sea during these campaigns. Observations from

111 TRAQA and SAFMED have shown that in the Western basin pollution plumes extend as far

112 as hundreds of km from the coastline and reach up to ~4000 m, presenting a complex

113 stratified structure, and pollution plumes show a large heterogeneity in terms of composition,

114 origin, and lifetime.

115 Following these observations, we may ask: does the heterogeneity in pollution plume

116 composition, origin, and lifetime as observed in Di Biagio et al. (2015) induce heterogeneity

117 on the optical properties (in particular the single scattering albedo) of pollution aerosols in

118 this part of the basin? And, if observed, does this heterogeneity on the optical properties

119 influence the aerosol DRE? Is it necessary to take it into account to better evaluate the aerosol

120 radiative impact in the Western Mediterranean?

121 With the aim of answering these questions, in this paper we analyse data of the optical

122 properties (spectral scattering and absorption coefficients, and single scattering albedo) and

123 size distributions of pollution aerosols measured over the Western Mediterranean basin

124 during TRAQA. SAFMED observations have been excluded here given that only limited data

125 on the aerosol optical properties are available from this campaign. The objective of the paper

126 is twofold: to provide a new dataset of aerosol single scattering albedo values which can be

127 representative of the polluted aerosols over the Western basin, and investigate the sensitivity

128 of the aerosol direct DRE to the variability of this parameter.

129

130

131

132   **2. Overview of flights during the TRAQA campaign**

133   The TRAQA campaign took place in the period 20 June – 13 July 2012. Instruments were

134   installed on board the SAFIRE (Service des Avions Français Instruments pour la Recherche

135   en Environnement, http://www.safire.fr/) tropospheric aircraft ATR-42, based in Toulouse

136   (43° 36' N, 1° 26' E, France). A total of seventeen flights, most often two flights per day,

137   with intermediate stops in different airports in southern France and Corsica, were performed

138   (flight numbers V16 to V32). The majority of flights were over the sea, with some exceptions

139   investigating inland areas in southern France. The flight altitude for the ATR-42 ranged

140   between a minimum of ~60 m to a maximum of ~5000 m above sea level (a.s.l.), and the

141   maximum flight time was 4 h. The general flight strategy consisted of legs at constant altitude

142   to sound the vertical structure by lidar observations, vertical ascents/descents to describe the

143   vertical atmospheric column and identify the main aerosol plumes, followed by straight

144   levelled runs (SLRs) within the detected aerosol layers. In the present study we will

145   exclusively consider measurements acquired during SLRs, since only during these phases the

146   whole set of aerosol optical properties (scattering and absorption coefficients) were

147   measured. A total of 21 SLRs were performed over the sea surface or inland close to the

148   coastline and will be considered in this study. Figure 1 and Table 1 summarise the

149   geographical location, time, and altitude of these 21 SLRs. As indicated in Table 1 each SLR

150   was about 15-20 min long. At the cruise speed of the ATR (93 ms^{-1}), this integration time

151   corresponds to about 100 km.

152

153   **3. Measurements and methods**

154   **3.1 Aircraft observations**

155   Aerosol sampling on the ATR-42 was performed using the AVIRAD system. AVIRAD is an

156   iso-axial and iso-kinetic inlet which samples air at a volumetric flow of ~350 L min^{-1}. The

157   50% passing efficiency of the inlet is 12 μm diameter. Various lines depart from AVIRAD to

158   connect to different instruments for the measurement of the aerosol physico-chemical and

159   optical properties. Additionally, several sensors for the measurements of the atmospheric

160   composition were installed on the ATR-42 aircraft as basic equipment. A brief description of

161   the different in situ measurements considered in this study from the AVIRAD system and the

162   ATR-42 equipment and their data analysis is reported in the following.

163   -   The aerosol scattering coefficient (σ_s) at 450, 550, and 700 nm has been measured by a 3-

164   wavelengths integrating nephelometer (TSI Inc., model 3563, 6s resolution). The

165 nephelometer was calibrated prior the campaign by using air and CO_2 as reference gases.

166 Nephelometer measurements have been corrected for angular truncation and Lambertian

167 non-idealities by applying the formula by Anderson and Ogren (1998), appropriated to

168 submicron aerosols which we expected in the pollution plumes sampled during the

169 campaign. The measurement uncertainty on σ_s, calculated taking into account for the

170 photon counting, gas calibration, and angular corrections uncertainties, is estimated to be

171 lower than 10% at the three wavelengths. Averages of the scattering coefficient are

172 calculated over the different SLRs. The uncertainty on the SLR average values is

173 estimated as the combination of the measurement uncertainty and the standard deviation

174 along each individual run. For each SLR, the particle scattering Ångström exponent (SAE)

175 has been calculated as the power law fit of the measured scattering coefficients versus

176 wavelength to extrapolate the scattering coefficient at other wavelengths than those of

177 operation.

178 The nephelometer measured the scattering coefficient in dry air conditions. This is due to

179 the heating of the airflow while entering the aircraft cabin and the temperature increase in

180 the sensing volume of the instrument due to illumination. The relative humidity measured

181 during the flights inside the nephelometer cavity was <25% in more than 90% of cases,

182 with values up to ~40% occasionally observed <200 m over the sea surface.

183 - The aerosol absorption coefficient (σ_{abs}) at 370, 470, 520, 590, 660, 880, and 950 nm has

184 been measured by a 7-wavelengths aethalometer (Magee Sci., model AE31, 2min

185 resolution). The principle of operation of the aethalometer consists in measuring the

186 attenuation of light through an aerosol-laden filter compared to that of another portion of

187 the filter which is unexposed to the air flow and is used as a reference (Weingartner et al.,

188 2003). To yield the aerosol absorption coefficient, the spectral attenuation $\sigma_{ATT}(\lambda)$

189 measured by the aethalometer has been corrected following the procedure described by

190 Collaud Coen et al. (2010):

191
$$\sigma_{abs}(\lambda) = \frac{\sigma_{ATT}(\lambda) - \alpha(\lambda)\overline{\sigma_s(\lambda)}}{C_{ref}R(\lambda)} \quad (1).$$

192 The different terms in equation 1 are: (i) $\alpha(\lambda)\overline{\sigma_s(\lambda)}$ or "scattering correction". In this work

193 $\alpha(\lambda)$ has been calculated with the formula by Arnott et al. (2005) and varies between 0.02

194 and 0.07, while $\overline{\sigma_s(\lambda)}$ is the average of the scattering coefficient along the considered SLR

195 extrapolated at the aethalometer wavelengths; (ii) C_{ref} or "multiple scattering correction".

196   C_{ref} is set to 2.14 ± 0.21 (wavelength-independent) following Weingartner et al. (2003);

197   (iii) $R(\lambda)$ or "shadowing effect correction". $R(\lambda)$ depends on the charge and

198   absorptivity properties of the sampled aerosol and can be calculated as a function of the

199   particle single scattering albedo (ω). In this study, because of the absence of an

200   independent determination of ω, we used an estimated "first-guess" single scattering

201   albedo (ω^*) to calculate R. This has been determined as the ratio of the measured

202   scattering (σ_s) to extinction ($\sigma_s + \sigma^*_{abs}$) coefficients, with σ^*_{abs} corrected for the scattering

203   and the multiple scattering corrections, but not for the shadowing effect. The obtained

204    $R(\lambda)$ varies between 0.75 and 1 for ω^* between 0.75-0.99 at 370 nm and 0.70-0.99 at 950

205   nm. The whole uncertainty on the absorption coefficient has been estimated with the

206   propagation error formula taking into account for the different factors in Eq. (1) and varies

207   between 11-36% at 370 nm and 12-70% at 950 nm.

208   It has to be noticed that an enhanced absorption at single wavelengths has been observed

209   in several cases for the aethalometer. This is possibly due to the absorption on the exposed

210   filter of gases or volatile compounds absorbing at some of the instrument operating

211   wavelengths (Weingartner et al., 2003). These anomalous points have been accurately

212   selected and screened from the dataset. As a result of this screening, data in

213   correspondence of only 60% of the considered SLRs are available for aerosols analyses.

214   The measured aerosol scattering and absorption coefficients have been used to calculate

215   the particle spectral single scattering albedo (ω) between 370 and 950 nm as:

216
$$\omega(\lambda) = \frac{\sigma_s(\lambda)}{\sigma_s(\lambda) + \sigma_{abs}(\lambda)} \qquad (2).$$

217   The uncertainty on ω has been calculated with the propagation error formula and varies

218   between 0.02 and 0.04 at all wavelengths.

219   Additionally, for each SLR for which aethalometer data are available, the particle

220   absorption Ångström exponent (AAE) has been calculated as the power law fit of the

221   measured absorption coefficients versus wavelength.

222   -   The aerosol number size distribution ($dN/dlogD_g$) has been measured by two different

223   optical particle spectrometers: the passive cavity aerosol spectrometer probe (PCASP,

224   model 100-X, 1-s resolution, 31 size classes between 0.1 and 3.0 µm diameter, operating

225   wavelength 632.8 nm), and the optical particle spectrometer SkyGRIMM (GRIMM Inc.,

226   model 1.129, 6-s resolution, 32 size classes between 0.3 and 32 µm diameter, operating

227   wavelength 655 nm). For both the PCASP and the SkyGRIMM, the measured sphere-

228   equivalent optical diameter has been converted in a sphere-equivalent geometrical

229   diameter (D_g) by taking into account the complex refractive index of the sampled aerosol

230   (Liu and Daum, 2000). Calculation are performed by fixing the imaginary part of the

231   refractive index at 0.01, thus representing a medium absorbing aerosol, while varying the

232   real part between 1.50 and 1.72, following the range of variability found in the literature

233   for pollution aerosols in the Mediterranean (see Di Biagio et al., 2015 for further details).

234   D_g is then set at the mean ± one standard deviation of the values obtained for the different

235   n. After refractive index correction the D_g ranges for the PCASP and the SkyGRIMM

236   become 0.10-4.47 and 0.28-65.80 µm, with an uncertainty between 1 and 25%. The

237   smallest and the largest size bins of both instruments, for which the minimum and

238   maximum edges respectively are not defined, have been excluded from the datasets, thus

239   reducing the PCASP and SkyGRIMM D_g ranges to 0.11-4.17 µm and 0.31-56.21 µm,

240   respectively.

241   Corrected data from the PCASP and the SkyGRIMM are then merged to obtain the aerosol

242   size distribution over a larger size range. The two instruments superimpose in a large

243   interval covering the diameter range ~0.31-4.17 µm. In this interval the PCASP and the

244   GRIMM show a good agreement below 0.4 µm and above 1.0 µm (less than ~10%

245   difference), while significant differences are observed in the 0.4-1.0 µm range where the

246   PCASP underestimates the SkyGRIMM measurements by more than ~50%. This

247   difference is of great relevance in terms of optical properties because particles in the 0.4-

248   1.0 µm size interval are very efficient for interaction with shortwave radiation. With the

249   aim of understanding which of the two instruments measures correctly in the 0.4-1.0 µm

250   range we have performed an optical test, which consisted in calculating with Mie theory

251   the scattering coefficient at 450, 550, and 700 nm based on the PCASP and SkyGRIMM

252   size data, and then in comparing it with simultaneous nephelometer measurements. Optical

253   calculations have been performed by fixing the complex refractive index at 1.6-0.01i, so at

254   the mean of the range of values reported in the literature for pollution aerosols (Ebert et

255   al., 2002 and 2004; Mallet et al., 2003 and 2011; Müller et al., 2002; Raut and Chazette,

256   2008). SLRs characterized by a low variability in terms of scattering coefficient and

257   particle concentration have been selected. The results of the optical test indicate that in the

258   0.4-1.0 µm range the size distribution of the SkyGRIMM is more accurate since it permits

259   to most closely reproduce nephelometer observations (<5% mean difference between

260   calculations and observations at the three wavelengths, compared to differences up to 15-

261   21% if PCASP data are used in the 0.4-1.0 µm size range). Thus, a combined PCASP-

262   SkyGRIMM number size distribution $dN/dlogD_g$ in the 0.11 to 56.21 µm diameter range

263   has been calculated by considering PCASP data up to 0.31 µm and SkyGRIMM data

264   above. Together with the number size distribution, for each SLR also the volume size

265   distribution $dV/dlogD_g = \pi/6\, D_g^3\, dN/dlogD_g$ has been calculated.

266   Nonetheless, due to a technical problem, SkyGRIMM data were only available below

267   ~350 m (~970 hPa).

268   -   The total particle number concentrations in the Aitken (4 nm-0.1 µm; dN_{Aitken}) and

269   accumulation (0.1-1.0 µm; dN_{Acc}) modes have been calculated by combining condensation

270   particle counter measurements of particle concentration in the 0.004 − 3 µm range (CPC,

271   TSI Inc., model 3775, 5-s resolution) and size distribution data. Due to the fact that above

272   350 m the SkyGRIMM is not available, only PCASP data are used in the calculations of

273   dN_{Aitken} and dN_{Acc} over the whole altitude range. dN_{Aitken} is estimated as the difference

274   between CPC concentration and the integral of PCASP data between 0.1 and 3.0 µm,

275   while dN_{Acc} is obtained by integrating the PCASP number concentrations in the 0.1-1.0

276   µm interval. The underestimation of the PCASP number concentration between 0.4 and

277   1.0 µm, as discussed above, is estimated to induce a ~20% underestimation of the dN_{Acc}

278   calculated here, whilst it has almost a negligible impact on dN_{Aitken}. The dN_{Acc} and dN_{Aitken}

279   obtained in correspondence of each SLR have been used to calculate the Aitken-to-

280   accumulation ratio dN_{Aitken}/dN_{Acc}.

281   -   The carbon monoxide (CO) and ozone (O_3) mixing ratios have been measured by the

282   MOZART instrument (CO, 30-s resolution and ±5% nominal uncertainty, O_3, 4-s

283   resolution and ±2% nominal uncertainty) (Nedelec et al., 2003). Starting from the

284   measured O_3 and CO, the ozone enhancement ratio ($\Delta O_3/\Delta CO$) has been calculated, i.e.

285   the ratio of the ozone to carbon monoxide variations compared to their baseline values. A

286   background value of ~70 ppbv in the boundary layer and ~60 ppbv in the free troposphere

287   has been used for CO, while the background has been set at ~30 ppbv for O_3 at all levels

288   (Di Biagio et al., 2015). $\Delta O_3/\Delta CO$ data have been used together with dN_{Aitken}/dN_{Acc} to

289   retrieve information on the age of the sampled air masses, as discussed in Di Biagio et al. (

290   2015).

291   In order to compare SLRs measurements obtained at different altitudes, the data analysed

292   here are reported to standard temperature and pressure (STP) using T=293.15 K and

293   P=1013.25 hPa. In this case, the scattering and absorption coefficients are scaled to STP

294   conditions and the particle concentrations (in number or volume) are given as particles per

295   standard cm^{-3} (scm^{-3}). Where not explicitly indicated, data refer to STP conditions.

296   In Table 2 we summarize main information and uncertainties for the different aerosol

297   instruments considered in this study.

298

299   **3.2 Boundary layer height estimation**

300   The planetary boundary layer (BL) top height has been estimated from meteorological

301   observations (temperature, T, potential temperature, θ, and relative humidity, RH) for each

302   vertical sounding performed during TRAQA flights (see Di Biagio et al., 2015). The

303   boundary layer top height is between 730 and 1500 m, with an average of ~1000 m. The

304   location of each SLR, so if it is within the boundary layer or in the free troposphere, has been

305   determined based on the planetary boundary layer top height estimated from the closest

306   vertical sounding performed during each flight.

307

308   **3.3 Tracking the origin of the sampled air masses**

309   As discussed in Di Biagio et al. (2015), aerosol observations during TRAQA were mostly

310   influenced by pollution/anthropogenic particles exported from different sources around the

311   basin (Northern Italy/Po Valley, Southern France, Barcelona area). The Lagrangian trajectory

312   model FLEXPART (FLEXible PARTicle dispersion model, Stohl et al., 1998), adapted for

313   the WRF (Weather Research and Forecasting) meteorological input (Brioude et al., 2013)

314   has been used here to track the origin of air masses sampled during SLRs. Five-day three-

315   dimensional back-trajectories have been calculated using the WRF meteorological output at a

316   30 km horizontal resolution and 28 vertical model levels up to 50 hPa. The model specific

317   humidity and potential vorticity is also interpolated along the trajectory path. Based on

318   FLEXPART simulations, data for the different SLRs have been separated as a function of the

319   origin of the sampled air masses. Three different sectors have been defined: the Western

320   sector, which includes trajectories coming from the Atlantic Ocean and travelling over France

321   or northern Spain before reaching the Western basin; the Eastern sector, including air mass

322   trajectories from continental Europe that have travelled over northern Italy-Po Valley before

323   entering the basin; and the Open Sea sector, which consists of trajectories coming from the

324   Western or Eastern sectors which have experienced at least 2 days of subsidence over the sea

325   in the Western basin and thus can be taken as representative of the regional background

326   aerosol or local pollution sources, i.e. ship emissions. The three different selected Sectors are

327   shown in Fig. 1, while Table 1 also reports the identified Sector of origin for the air masses

328   sampled during the different SLRs. As discussed in Di Biagio et al. (2015), several flights

329   were affected by dust particles exported over the basin from Northern Africa. SLRs data

330   dominated by dust have been identified based on the combined analysis of back-trajectories,

331   lidar profiles and optical data, and have been excluded from the dataset. However, for some

332   SLRs, the possible mixing of dust aerosols with pollution particles cannot be a priori

333   excluded.

334

3.4 Radiative model calculations

336   Radiative transfer calculations have been performed to estimate the instantaneous aerosol

337   direct radiative effect in the shortwave spectral range for different cases and in clear-sky

338   conditions. The objective of the calculations is to test the sensitivity of the DRE to the

339   variability of the aerosol optical properties, in particular the single scattering albedo, as

340   observed in this study. The GAME radiative transfer model (Dubuisson et al., 1996 and

341   2006) has been used in this study to compute the vertical profiles of downward and upward

342   shortwave irradiances over the 0.28-3.0 μm spectral range. The model calculates radiances

343   and irradiances at various atmospheric levels at 400 cm^{-1} spectral resolution between 0.28 and

344   0.5 μm and 100 cm^{-1} resolution between 0.5 and 3 μm. Spectral absorption by principal

345   atmospheric gases (H_2O, CO_2, O_3, CH_4, N_2O, O_2) is taken into account in the model. The

346   discrete ordinate method (Stamnes et al., 1988) with twelve streams is used in the simulations

347   to describe multiple scattering. Simulations have been performed with and without aerosols

348   by fixing the solar zenith angle (θ) at 60°, i.e. at about the mean of the diurnal value at the

349   latitudes of north-Western Mediterranean, and for a mid-latitude climatological summer

350   meteorological profile. The aerosol optical properties that are used as input in the GAME

351   radiative code are the spectral variation of the optical depth (τ), the asymmetry parameter (g)

352   and the single scattering albedo (ω). The difference of the net shortwave fluxes (downward

353   minus upward irradiances) with and without aerosols at the surface and at TOA is used to

354   estimate the aerosol DRE at these two levels. The atmospheric DRE is then calculated as the

355   difference between the TOA and the surface values. Finally, the ratio of the DRE to the

356   aerosol optical depth at 500 nm, i.e. the aerosol forcing efficiency (FE), is obtained. The

357   shortwave heating rate at the altitude z is also calculated as:

358
$$\frac{\partial T}{\partial t} = -\frac{1}{\rho C_p}\frac{\partial F(z)}{\partial z} \quad (3)$$

359   where T is the air temperature, ρ is the air density, C_p is the specific heat of the air, and $F(z)$

360   is the net flux at the altitude z.

361

362   **4. Results**

363   **4.1 Overview over the different SLRs**

364   Figure 2 shows the averages altitude, spectral scattering (σ_s) and absorption (σ_{abs})

365   coefficients, scattering and absorption Ångström exponent (SAE and AAE, respectively),

366   ozone enhancement factor ($\Delta O_3/\Delta CO$), and Aitken-to-accumulation ratio (dN_{Aitken}/dN_{Acc})

367   measured for the different SLRs during TRAQA.

368   As shown in Fig. 2 and Table 1, the large majority of the SLRs were performed within the

369   boundary layer at an altitude <1000 m. Only four SLRs (V25_R2, V25_R3, V26_R1, and

370   V30_R1) measured aerosols in the free troposphere between 1800 and 3500 m. The sampled

371   aerosols originated in each of the three different source sectors identified based on

372   FLEXPART back-trajectories (Western, Easter, and Open Sea), with a larger number of cases

373   from the Western sector compared to the Eastern and the Open Sea areas.

374   For all the different cases, the measured scattering coefficient is in the range 16-73 Mm^{-1} at

375   450 nm and 8-30 Mm^{-1} at 700 nm. The absorption coefficient is generally below 10 Mm^{-1} at

376   all wavelengths, with the exception of V27_R1 and V32_R1 for which values up to ~20 Mm^{-1}

377   at 370 nm have been measured. For these two cases also the highest values of the particle

378   concentration in the accumulation mode (~1700-2200 # cm^{-3}, not shown) and among the

379   highest values of the scattering coefficient are measured. For all cases, both σ_s and σ_{abs}

380   decrease with the wavelength. The pronounced spectral variability of σ_s, in particular,

381   indicates the dominance of pollution/anthropogenic fine particles in the sampled plumes.

382   The SAE varies between 0.96 and 1.94, while the AAE varies between 0.92 and 1.65, with an

383   average of ~1.20. The AAE has been not calculated for few cases with very low values of the

384   absorption coefficient (σ_{abs} at 370 nm < 1.5 Mm^{-1}). Both the SAE and the AAE obtained in

385   this study fall in the range of variability indicated by several authors to identify

386   pollution/anthropogenic aerosols or pollution mixed with other aerosol types in the

387   Mediterranean basin (SAE>1-1.5, and AAE~1-1.5; Pace et al., 2006; Toledano et al., 2007;

388   Mallet et al., 2013). Values of AAE larger than unity, in particular, might suggest the possible

389   mixing of pollution with brown carbon or dust particles over the basin (Russell et al., 2010;

390   Mallet et al., 2013).

391   For all the measured SLRs the $\Delta O_3/\Delta CO$ and the dN_{Aitken}/dN_{Acc} ratios vary in the range 0.37-

392   1.02 and 1-50, respectively, for O_3 and CO varying between 24-78 and 69-136 ppbv and

393   dN_{Aitken} and dN_{Acc} between 320-22500 and 100-2170 # cm^{-3}. $\Delta O_3/\Delta CO$ and the dN_{Aitken}/dN_{Acc}

394   are linked to the photochemical (rate of ozone formation) and physical (rate of Aitken to

395   accumulation particle conversion) processes responsible for the ageing of the aerosol plumes.

396   The range of measured values here includes both cases with high dN_{Aitken}/dN_{Acc} and low

397    $\Delta O_3/\Delta CO$, typical of fresh plumes, and cases with low dN_{Aitken}/dN_{Acc} and high $\Delta O_3/\Delta CO$,

398   indicative of more aged air masses (Di Biagio et al., 2015).

399   The summary of these observations suggests that the set of SLRs measurements considered in

400   this study can be considered representative of a wide range of different atmospheric

401   conditions occurring over the basin both in terms of sources, loadings, and lifetime for

402   pollution aerosols.

403

4.2 Particle size distributions

405   Figure 3 shows the mean and the range of variability of the number and volume size

406   distributions measured during horizontal SLRs within pollution layers during TRAQA. Data

407   refers only to cases at <350 m altitude within the boundary layer. The absolute uncertainty on

408   the measured concentration, as also reported in Table 2, is ~15% for particle diameters below

409   0.31 μm and ~10% at larger sizes. The grey shading indicates considerable variability in the

410   number concentration of the size distributions, of approximately one order of magnitude for

411   much of the size range measured. This reflects the relative wide range of aerosol loadings

412   encountered during the campaign.

413   The measured number size distribution from each SLR has been fitted with multi-mode

414   lognormal functions:

415
$$\frac{dN}{d\log D_g} = \sum_i \frac{N_{tot,i}}{\sqrt{2\pi}\log\sigma_{g,i}} \left(-\frac{\left(\log D_p - \log D_{g,i}\right)^2}{2\log^2\sigma_{g,i}} \right) \quad (4).$$

416   For each mode I, N_{tot} represents the total aerosol number concentration, D_g the median

417   diameter, and σ_g the geometric standard deviation. The logarithm refers to base 10. Size data

418   were fitted automatically using the MPCURVEFIT IDL routine available at

419   http://www.physics.wisc.edu/~craigm/idl/fitting.html. Since the aim of the fitting is to

420   describe as closely as possible the measured number size distributions for subsequent optical

421   calculations (Sect. 4.4), up to seven modes were used to fit the data. The parameters of the

422   lognormal fits are reported in Table 3. The first mode of the size distribution is generally at

423   0.13-0.14 µm, whilst the largest mode is between ~5 and 8 µm for the different cases.

424

425   **4.3 Spectral single scattering albedo: variability as a function of air mass origin and**

426   **height**

427   Figure 4 shows the spectral ω for the different SLRs considered in this study. Data have been

428   separated based on the origin of the sampled air masses. The single scattering albedo varies in

429   the range 0.84-0.98 at 370 nm and 0.70-0.99 at 950 nm and generally decreases with the

430   wavelength, as it is typical for pollution particles (Dubovik et al., 2002). Only in two cases

431   (V19_R1 and V30_R2) the single scattering albedo increases with wavelength. For these

432   cases also very high values of ω are observed (0.92-0.97 for V19_R1 and 0.98-1.0 for

433   V32_R2), which may suggest the possible mixing of pollution with sea spray. The lowest

434   values of the single scattering albedo are measured for V27_R1 (0.84-0.70 between 370 and

435   950 nm) sampled at ~160 m and originated in the Open Sea sector. Data in Fig. 2 also

436   indicate for V27_R1 very low values of $\Delta O_3/\Delta CO$ (~0.37) and a relatively high

437   dN_{Aitken}/dN_{Acc} (~7), which suggests that V27_R1 is a fresh plume possibly associated to local

438   emissions, i.e. ship plumes, over the basin. If we exclude V27_R1, the range of measured

439   values appears comparable (within error bars) for the three considered sectors (Western,

440   Eastern, and Open sea; ω between 0.88 and 0.98 at 370 nm and 0.83 and 0.99 at 950 nm.

441   The vertical variability of ω, together with dN_{Aitken}/dN_{Acc}, $\Delta O_3/\Delta CO$, SAE, and AAE, is

442   shown in Fig. 5 for the different considered cases. With the only exception of V27_R1, for

443   which the lowest values are observed below 200 m, the single scattering albedo does not

444   show a clear trend with height, with a similar range of values measured in the boundary layer,

445   below ~1000 m, and in the free troposphere up to ~3500 m. As for ω, the AAE does not

446   significantly vary with height. At the same time, dN_{Aitken}/dN_{Acc} and SAE decrease with

447   height, with a concurrent slight $\Delta O_3/\Delta CO$ increase, which may suggest an increase of plume

448   age with height. The ensemble of these observations seems to indicate that, for our observed

449   cases, the absorptivity properties of the sampled plumes do not depend on altitude and

450   associated air mass age of the plume. It should be pointed out, however, that the majority of

451   cases considered here have been sampled below 1000 m, so in the boundary layer, and the

452   statistics in the free troposphere is only limited to a few events.

453 Values of the single scattering albedo measured in this study are comparable with values

454 reported at several other sites in the Central and Western Mediterranean region for pollution

455 aerosols (Mallet et al., 2003 and 2013; Meloni et al., 2006; Saha et al., 2008; Di Biagio et al.,

456 2009; Pandolfi et al., 2011). The single scattering albedo from these studies is observed to

457 vary in the range 0.84-0.95 at 440 nm, 0.76-0.98 at 500-550 nm, and 0.80-0.87 at 870 nm.

458 Compared with the literature, larger and lower values are obtained in the present study for

459 few cases mostly influenced by sea spray and local fresh emissions, respectively.

460

461 **4.4 Optical closure and estimation of the aerosol complex refractive index**

462 As discussed in the previous section, the single scattering albedo of pollution aerosols shows

463 a relatively large variability. Here we investigate the impact of this variability on the complex

464 refractive index (m=n-ik) of the particles.

465 For eight selected SLRs for which both complete optical (scattering and absorption

466 coefficients, and single scattering albedo) and size distribution measurements were available,

467 the aerosol spectral complex refractive index has been estimated by optical closure study.

468 These cases correspond to V19_R1, V21_R1, V21_R3, V23_R2, V27_R1, V31_R1,

469 V32_R1, V32_R3 sampled within the boundary layer at <350 m altitude. The optical closure

470 consisted in recalculating the spectral scattering σ_s and absorption σ_{abs} coefficients measured

471 for each SLR by using the measured size distribution as input and by varying the real (n) and

472 imaginary (k) parts of the complex refractive index in the calculations. Then, n and k are

473 fixed when the best agreement between measurements and calculations is found. Optical

474 calculations have been performed using Mie theory for spherical particles. The

475 Mie_single.pro IDL routine available at http://www.atm.ox.ac.uk/code/mie/mie_single.html

476 has been used. In the calculations the real part of the refractive index is varied in the range

477 1.30-1.80 at steps of 0.01, while the imaginary part in the range 0.001-0.1 at steps of 0.001,

478 for a total of 5100 inversions for each SLR dataset. The uncertainty on the real and imaginary

479 parts of the refractive index has been estimated with a sensitivity study. To this purpose, the

480 values of n and k are also obtained by using as input the observed σ_s, σ_{abs}, and $\dfrac{dN}{d\log D_g}$ plus

481 or minus one standard deviation on their measurement. The deviations of the values of n and

482 k retrieved in the sensitivity study with respect to those obtained in the first inversions are

483 assumed to correspond to the one standard deviation uncertainty. The estimated uncertainty is

484 <5% for n and ~25-30% for k.

485   The comparison of the measured and calculated σ_s and σ_{abs} are shown in Fig. 6, while the

486   retrieved real and imaginary parts of the refractive index for the different SLRs are reported

487   in Fig. 7. Data in Fig. 7 are also compared to the real and imaginary parts of the refractive

488   index for the single components (insoluble, water soluble, soot, and sea salt) considered in

489   the OPAC model (Optical Properties of Aerosols and Clouds, Hess et al., 1998) to represent

490   continental, urban and maritime polluted aerosols.

491   As shown in Fig. 6, a very good agreement is found between the calculated and the measured

492   scattering and absorption coefficients, with an average difference of less than 5% for both σ_s

493   and σ_{abs}. For our analysed cases n and k vary in the range 1.67-1.75 and 0.003-0.038 at 370

494   nm and 1.41-1.75 and 0.002-0.068 at 950 nm, respectively. The imaginary part of the

495   refractive index slightly increases with wavelength, while a decrease is observed for the real

496   part in most cases. Highest values of k are obtained for V27_R1, which also shows the

497   absolute lowest values of ω in our dataset (0.84-0.70), followed by V32_R1 and V32_R2,

498   which also present relatively low values of ω (0.95-0.83). The lowest k, as well as among the

499   lowest n, is instead obtained for V19_R1 (ω=0.92-0.96). The comparison of our data with

500   OPAC values for single components suggests that in most cases particles are composed of a

501   mixing of insoluble and water soluble components, with possible contributions of soot

502   (V27_R1) ad sea salt (V19_R1). The results of the complex refractive index obtained in this

503   study are in agreement with previous estimates obtained for pollution aerosols in continental

504   Europe (n~1.50-1.72 and k~0.001-0.1 for UV-visible wavelengths e.g. Ebert et al., 2002,

505   2004; Müller et al., 2002; Mallet et al., 2003, 2011; Raut and Chazette, 2008). Larger values

506   of both n and k are instead obtained here compared to AERONET retrievals at different sites

507   in the Western Mediterranean (1.38-1.46 for n and 0.003-0.01 for k at 440 and 670 nm;

508   Mallet et al., 2013).

509   Figure 8 shows the results of the correlation analysis between the single scattering albedo and

510   the complex refractive index obtained for the analysed cases. For the real part, the range of

511   retrieved n values is larger (1.41-1.70) for ω greater than ~0.95, while as the single scattering

512   albedo decreases the real part converges to ~1.70-1.75 at all wavelengths. A strong

513   correlation is observed between ω and k at all wavelengths, that is the lower the single

514   scattering albedo, the higher the imaginary part. A linear regression fit was applied to the ω-k

515   datasets at the seven wavelengths (R^2=0.83-0.95 at all wavelengths for the different fits). The

516   intercept for all cases is lower than 1 (0.94-0.97), with lowest values (0.94) obtained at 880

517   and 950 nm. This is possibly associated to a slight underestimation of ω which, especially at

518   these wavelengths, is difficult to determine given the high uncertainty on the particle

519   absorption coefficient. Another source of uncertainty is the size distribution, which influences

520   the results of Mie calculations, and thus has a direct impact on the refractive index retrieval.

521

4.5 Influence of the single scattering albedo variability on the aerosol direct shortwave

radiative effect (DRE)

524   Radiative transfer model calculations with the GAME model have been performed with the

525   aim of investigating the impact of the variable optical properties, and in particular the single

526   scattering albedo, on the shortwave direct radiative effect of pollution particles in the Western

527   Mediterranean basin.

528   Simulations have been performed by considering three different vertical aerosol profiles,

529   based on observations reported by Di Biagio et al. (2015): i. aerosols only confined in the BL

530   (whose altitude is fixed at 1000 m, in the mean of observations during TRAQA); ii. 50% of

531   the aerosol optical depth in the BL and 50% in the FT (which is considered to extend between

532   1000 and 4000 m); iii. 20% of the aerosol optical depth in the BL and 80% in the FT. For the

533   different cases we fixed the total aerosol optical depth at 0.2 at 550 nm, which corresponds to

534   the mean of observations obtained over the Western basin during TRAQA (Di Biagio et al.,

535   2015). However, results will be given as FE so they are independent on the chosen optical

536   depth. We assume a uniform aerosol distribution and constant optical properties within the

537   BL and the FT for the three different considered profiles. This assumption comes from the

538   observations of the present study, which do not evidence any significant change of the

539   aerosol properties with height. Aerosol spectral optical properties, both in the BL and in the

540   FT up to 4000 m, are assumed from observations, as explained in the following.

541   The GAME model requires as input the aerosol optical depth, single scattering albedo, and

542   asymmetry factor at 7 wavelengths between 330 and 1500 nm. The spectral optical depth

543   between 330 and 1500 nm is extrapolated from the fixed value of 0.2 at 550 nm by assuming

544   a Ångström exponent of 1.5, in the mean of our observations for pollution aerosols (see Fig.

545   2). For the single scattering albedo, we considered 3 different sets of values which correspond

546   to the minimum, maximum, and mean of the values observed in this study (the absolute

547   minimum for V27_R1 has been excluded for calculations since it represents an outlier in our

548   data). The ω values at 370-950 nm as obtained from experimental data are then extrapolated

549   at the 7 GAME wavelengths (Table 4). The asymmetry factor is calculated from Mie theory

550   based on the refractive index values and size distribution data for the eight cases considered

551   in the previous Section. The spectral variation of g used in the radiative transfer calculations

552   is estimated as the mean of the values obtained for these eight cases extrapolated at the 7

553   GAME wavelengths. The obtained g varies between 0.60 at 330 nm and 0.51 at 1500 nm.

554   These values are consistent with previous estimates of g obtained for pollution aerosols over

555   the Mediterranean basin (Meloni et al., 2006; Saha et al., 2008; Mallet et al., 2011).

556   Background stratospheric aerosols (above 12 km) are also taken into account for radiative

557   calculations; optical properties from the OPAC stratospheric aerosol model (Hess et al.,

558   1998) are assumed.

559   Finally, in addition to aerosol optical properties, the GAME model requires as input the

560   albedo of the surface (A_S) at 5 wavelengths between 448 nm and 2130 nm. In this study,

561   simulations are performed over the sea surface. The albedo of the sea surface is obtained

562   from Jin et al. (2004), which provide a parameterisation of A_S as a function of chlorophyll

563   concentration (Chl), wind speed (w), aerosol optical depth at 500 nm (τ), and the solar zenith

564   angle (θ). For this study A_S is estimated for Chl=0, w=6-9 m s^{-1}, τ=0.24 (extrapolated from

565   the value of 0.2 at 550 nm), and θ=60°, and it varies between 0.009 and 0.005 in the

566   considered 448-2130 nm spectral range.

567   Results of the radiative transfer simulations are shown in Fig. 9, which reports the FE at the

568   surface, TOA, and atmosphere (FE_S, FE_{TOA} and FE_{ATM}) for the maximum, mean, and

569   minimum of the single scattering albedo observed in this study. Results of the simulations are

570   mostly independent on the vertical distribution of the aerosols (less than ~5% changes for

571   FE_S, FE_{ATM}, and FE_{TOA} for the three different profiles used in the simulations), so the mean

572   of the results obtained for the three cases is reported in Fig. 9. The forcing efficiency varies

573   between -160 and -235 (FE_S), -137 and -92 (FE_{TOA}), and +23 and +143 (FE_{ATM}) W m^{-2} τ^{-1} for

574   ω varying between its maximum and minimum values. Estimates of the forcing efficiencies

575   in correspondence of the mean of ω are -198, -113, and +85 W m^{-2} τ^{-1} at the surface, TOA,

576   and atmosphere, respectively. The corresponding instantaneous shortwave heating rate at the

577   surface varies between 0.2 and 2.0 K day^{-1} for ω between its maximum and minimum.

578   As expected, the lower the single scattering albedo, the larger in absolute value the FE_S and

579   FE_{ATM} and the lower the FE_{TOA}. This is due to the impact of absorption on the amount of

580   radiation trapped in the atmosphere and transmitted towards the surface, which thus enhance

581   the radiative effect in the atmosphere and at the surface for decreasing ω. Conversely, the

582   larger the particle absorption, the lower the effect on the radiation reflected back to space,

583   and thus the decrease of the intensity of the cooling effect at the TOA. Changes in the single

584   scattering albedo of the particles between its maximum and minimum ($\Delta\omega$=0.1-0.2 at the

585   different wavelengths) determine about a 50% strengthening of the direct shortwave radiative

586   effect at the surface, and a reduction of ~30% the effect at the TOA. Consequently, the

587   atmospheric FE may vary up to an order of magnitude. These results thus highlight the

588   sensitivity of the DRE on the absorptivity properties of the particles, as well as the

589   importance of accurately reproducing the single scattering albedo of aerosols to correctly

590   evaluate their direct radiative effect.

591   The results of the present study are in quite good agreement with previous estimates of the

592   aerosol forcing efficiency for pollution aerosols in the Mediterranean area. FE_S, FE_{ATM}, and

593   FE_{TOA} obtained here compare well with data obtained in the Central Mediterranean by Di

594   Biagio et al. (2009, 2010), who provide estimates based only on observational data, i.e.

595   without any assumption on the aerosol optical properties. In these studies they report a

596   forcing efficiency of ~-200 and -164 W m^{-2} τ^{-1} at the surface and TOA at solar zenith angles

597   of 50°-60° for mixed aerosols (pollution plus sea salt particles). They estimate an increase in

598   absolute value of FE_S of about 20-40% due to a decrease of 0.1-0.2 of the single scattering

599   albedo (at 415 and 868 nm) of the aerosols, as well as a concurrent increase of FE_{TOA} of

600   about 10-40%. The observations obtained in this study fall in the range of variability reported

601   by Di Biagio et al. (2009, 2010). Our data also agree with estimates of Saha et al. (2008),

602   reporting for pollution aerosols measured in the French Mediterranean coast up to 40%

603   variability in the FE_S and FE_{TOA}, concurrently with 70% increase of FE_{ATM}, due to a ω

604   change of 0.15 at 525 nm. Conversely, our estimates at the surface and TOA are larger in

605   absolute value compared to data reported for continental Europe by Horvath et al. (2002),

606   who estimated a FE_S of ~-164 W m^{-2} τ^{-1} and a FE_{TOA} of -50 W m^{-2} τ^{-1} for polluted aerosols

607   with ω=0.90 at 520 nm, thus comparable with our mean values of single scattering albedo for

608   pollution aerosols.

609

610   **5. Conclusions**

611   In this study we have presented measurements of the spectral optical properties (scattering

612   and absorption coefficients and single scattering albedo) and particle size distributions for

613   pollution aerosols obtained over the remote sea in the Western Mediterranean basin during

614   the TRAQA campaign in summer 2012. The set of observations analysed in this study can be

615   assumed to be representatives of a wide range of different conditions that can be observed

616   over the basin, both in terms of pollution sources, aerosol loadings, and lifetimes of the

617   plumes. The detailed characterization of the spectral optical properties of pollution aerosols

618   in the Western basin was missing to date.

619   Observations from the present study show a large variability of the optical properties of

620   pollution aerosols over the basin, in particular of the spectral single scattering albedo. Values

621   of ω in the range 0.84-0.98 at 370 nm and 0.70-0.99 at 950 nm are observed in this study.

622   This variability of ω does not seem to be clearly linked neither to the particle origin, nor to

623   the altitude and associated ageing of the sampled plumes. The variability of ω reflects in a

624   large variability for the complex refractive index of pollution aerosols, which is estimated to

625   span in the range 1.41-1.75 for the real part and 0.002-0.068 for the imaginary part between

626   370 and 950 nm. The analysis of the complex refractive index suggests that possible

627   differences in terms of particle compositions can explain in part the observed variability of ω.

628   A large range of compositions has been however reported for pollution aerosols in Europe

629   and the Mediterranean basin (Mallet et al., 2003; Ebert et al., 2004; Pey et al., 2010; Piazzola

630   et al., 2012) and a more detailed analysis of the composition for the cases obtained in this

631   study should be addressed.

632   Based on the observations of the present study, the variability of optical properties for

633   pollution aerosols can arise from the combination of different factors, linked to the origin,

634   production mechanism, and ageing of the plumes along their lifetime, as well as the possible

635   mixing of different plumes with different characteristics. So, the inherent heterogeneity of

636   sources, coexistence of different air masses, and multiple physical and chemical processes

637   occurring in a complex environment such as the Western Mediterranean may give rise to this

638   inherent variability of the particle single scattering albedo.

639   This observed variability on ω has a large influence on the direct shortwave radiative effect

640   of pollution aerosols at the surface, TOA, and within the atmosphere. For instance, a change

641   of up to an order of magnitude (from +23 to +143 W m^{-2} τ^{-1} at 60° solar zenith angle) in the

642   atmospheric radiative effect is estimated due to the variability of the single scattering albedo

643   within the range of values observed in this study. The change in the amount of atmospheric

644   absorbed solar radiation may have a strong impact on the temperature profile and the

645   atmospheric thermal structure, with important consequences on several processes, such as

646   cloud formation and precipitations. The strong sensitivity of the DRE also at the surface, up

647   to 50% for varying ω, on its turn, may largely impact the rate of evaporation over the basin,

648   which is also a crucial component of the hydrological cycle (Nabat et al., 2015). Given the

649   large sensitivity of the Mediterranean area and the high risk of desertification for this region

650 (Giorgi and Lionello, 2008; IPCC, 2013) any factor possibly impacting the hydrological cycle

651 should be taken carefully into account by regional climate models. In this view, results from

652 the present study can be used to provide a constraint of the absorption properties of pollution

653 particles in the Western Mediterranean basin to use in regional modelling studies.

654 Constraining these properties constitutes a crucial step in order to better assess the role of

655 aerosols on the radiative balance of this region and to ameliorate the capability of making

656 projection on future climate changes.

657

658 **Author contributions**

659 J.-L. Attié, F. Ravetta, G. Ancellet, and P. Formenti designed the TRAQA experiment and

660 coordinated the campaign. C. Gaimoz, N. Grand, and C. Di Biagio operated the instruments

661 on board the ATR-42 during the flights. C. Di Biagio performed the data analysis with

662 contributions from L. Doppler and P. Formenti. S. Bucci and F. Fierli performed the

663 FLEXPART simulations. M. Mallet and P. Dubuisson provided the GAME code for radiative

664 calculations. C. Di Biagio wrote the manuscript with contributions from the co-authors.

665

666

667 **Acknowledgements**

668 All measurement presented here are from the Chemistry-Aerosol Mediterranean Experiment

669 project (ChArMEx, http://charmex.lsce.ipsl.fr), which is the atmospheric component of the

670 French multidisplinary program MISTRALS (Mediterranean Integrated Studies aT Regional

671 And Local Scales). ChArMEx-France was principally funded by INSU, ADEME, ANR,

672 CNES, CTC (Corsica region), EU/FEDER, Météo-France, and CEA. TRAQA was funded by

673 ADEME/PRIMEQUAL and MISTRALS/ChArMEx programmes and Observatoire Midi-

674 Pyrénées. C. Di Biagio thanks the Centre National des Etudes Spatiales (CNES) for financial

675 support.

676 The authors wish to thank the technicians, pilots and ground crew of SAFIRE (Service des

677 Avions Francais Instruments pour la Recherche en Environnement) for facilitating the

678 instrument integration and conducting flying operations. We thank S. Chevaillier, R. Loisil, J.

679 Pelon, and P. Zapf for their contribution during the campaign. We also wish to thank G. Siour

680 for his help to run the GAME radiative code.

681

682 **References**

683 Anderson, T. L. and Ogren, J. A.: Determining aerosol radiative properties using the TSI 3563
684   integrating nephelometer, Aerosol Sci. Technol., 29, 57–69, 1998.

685 Arnott, W., Hamasha, K., Moosm¨uller, H., Sheridan, P. J. , and Ogren, J. A.: Towards aerosol light-
686   absorption measurements with a 7-wavelength aethalometer: Evaluation with a photoacoustic
687   instrument and 3-wavelength nephelometer, Aerosol Sci. Tech., 39(1), 17–29, 2005.

688 Boucher, O., et al., Clouds and Aerosols. Stocker, T., & Qin, D. (eds), Climate Change 2013: The
689   Physical Science Basis. Contribution of Working Group I to the Fifth Assessment Report of the
690   Intergovernmental Panel on Climate Change. Cambridge Univ. Press, Cambridge, United
691   Kingdom and New York, NY, USA, 2013.

692 Brioude, J., Arnold, D., Stohl, A., Cassiani, M., Morton, D., Seibert, P., Angevine, W., Evan, S.,
693   Dingwell, A., Fast, J. D., Easter, R. C., Pisso, I., Burkhart, J., and Wotawa, G.: The Lagrangian
694   particle dispersion model FLEXPART-WRF version 3.1, Geosci. Model Dev., 6, 1889-1904,
695   doi:10.5194/gmd-6-1889-2013, 2013.

696 Collaud Coen, M., Weingartner, E., Apituley, A., Ceburnis, D., Fierz-Schmidhauser, R., Flentje, H.,
697   Henzing, J. S., Jennings, S. G., Moerman, M., Petzold, A., Schmid, O., and Baltensperger, U.:
698   Minimizing light absorption measurement artifacts of the Aethalometer: evaluation of five
699   correction algorithms, Atmos. Meas. Tech., 3, 457–474, doi:10.5194/amt-3-457-2010, 2010.

700 Di Biagio, C., di Sarra, A., Meloni, D., Monteleone, F., Piacentino, S., and Sferlazzo, D.:
701   Measurements of Mediterranean aerosol radiative forcing and influence of the single scattering
702   albedo, J. Geophys. Res., 114, D06211, doi:10.1029/2008JD011037, 2009.

703 Di Biagio, C., di Sarra, A., and D. Meloni, D.: Large atmospheric shortwave radiative forcing by
704   Mediterranean aerosol derived from simultaneous ground-based and spaceborne observations, and
705   dependence on the aerosol type and single scattering albedo, J. Geophys. Res., 115, D10209, doi:
706   10.1029/2009JD012697, 2010.

707 Di Biagio, C., Doppler, L., Gaimoz, C., Grand, N., Ancellet, G., Raut, J.-C., Beekmann, M.,
708   Borbon, A., Sartelet, K., Attié, J.-L., Ravetta, F., and Formenti, P.: Continental pollution in the
709   western Mediterranean basin: vertical profiles of aerosol and trace gases measured over the sea
710   during TRAQA 2012 and SAFMED 2013, Atmos. Chem. Phys., 15, 9611-9630, doi:10.5194/acp-
711   15-9611-2015, 2015.

712 Dubovik, O., Holben, B., Eck, T. F., Smirnov, A., Kaufman, Y. J., King, M. D., Tanré, D., and
713   Slutsker, I.: Variability of absorption and optical properties of key aerosol types observed in
714   worldwide locations, J. Atmos. Sci., 59, 590–608, 2002.

715 Dubuisson, P., Buriez, J. C. and Fouquart, Y.: High spectral resolution solar radiative transfer in
716   absorbing and scattering media: Application to the satellite simulation, J. Quant. Spectrosc. Radiat.
717   Transfer, 55, 103–126, 1996.

718 Dubuisson, P., Roger, J., Mallet, M., and Dubovik, O.: A Code to Compute the Direct Solar
719   Radiative Forcing: Application to An- thropogenic Aerosols during the Escompte
720   Experiment, Proc. In- ternational Radiation Symposium (IRS 2004) on Current Prob- lems
721   in Atmospheric Radiation, edited by: Fischer, H., Sohn, B.- J., and Deepak, A., Hampton,
722   127–130, 23–28 August 2004, Bu- san, Korea, 2006.

723 Ebert, M., Weinbruch, S., Rausch, A., Gorzawski, G., Hoffmann, P., Wex, H., and Helas, G.: The
724   complex refractive index of aerosols during LACE 98 as derived from the analysis of individual
725   particles, J. Geophys. Res., 107, D21, 8121, doi:10.1029/2000JD000195, 2002.

726 Ebert, M., Weinbruch, S., Hoffmann, P., and Ortner, H. M.: The chemical composition and complex
727   refractive index of rural and urban influenced aerosols determined by individual particle analysis,
728   Atmos. Environ., 38, 6531–6545, 2004.

729 Estellés, V., Martínez-Lozano, J. A., Utrillas, M. P., and Campanelli, M.: Columnar aerosol properties
730   in Valencia (Spain) by ground-based Sun photometry, J. Geophys. Res., 112, D11201,
731   doi:10.1029/2006JD008167, 2007.

732 Esteve, A. R., Ogren, J. A., Sheridan, P. J., Andrews, E., Holben, B. N., and Utrillas, M. P.: Sources
733   of discrepancy between aerosol optical depth obtained from AERONET and in-situ aircraft
734   profiles, Atmos. Chem. Phys., 12, 2987-3003, doi:10.5194/acp-12-2987-2012, 2012.

735 Giorgi, F., and Lionello, P.: Climate change projections for the Mediterranean region. Global Planet
736   Change, 63, 90-104. doi:10.1016/j.gloplacha.2007.09.005, 2008.

737 Gkikas, A., Houssos, E. E., Hatzianastassiou, N., Papadimas C. D., and Bartzokas, A.: Synoptic
738   conditions favouring the occurrence of aerosol episodes over the broader Mediterranean basin Q. J.
739   R. Meteorol. Soc. 138: 932–949, 2012.

740 Hess, M., Koepke, P., and Schult, I.: Optical properties of aerosols and clouds: The software package
741   OPAC, Bull. Am. Meteorol. Soc, 79, 831–844, 1998.

742 Horvath, H., Alados Arboledas, L., Olmo, F. J., Jovanovic, O., Gangl, M., Sanchez, C., Sauerzopf, H.,
743   and Seidl, S.: Optical characteristics of the aerosol in Spain and Austria and its effect on radiative
744   forcing, J. Geophys. Res., 107, 4386, doi: 10.1029/2001JD001472, 2002.

745 IPCC, 2013: Climate Change 2013: The Physical Science Basis. Contribution of Working Group I to
746   the Fifth Assessment Report of the Intergovernmental Panel on Climate Change [Stocker, T.F., D.
747   Qin, G.-K. Plattner, M. Tignor, S.K. Allen, J. Boschung, A. Nauels, Y. Xia, V. Bex and P.M.
748   Midgley (eds.)]. Cambridge University Press, Cambridge, United Kingdom and New York, NY,
749   USA, 1535 pp, doi:10.1017/CBO9781107415324.

750 Jin, Z., Charlock, T. P., Smith Jr., W. L., and Rutledge, K.: A parametrization of ocean surface
751   albedo, Geophys. Res. Lett., 31, L22301, doi:10.1029/2004GL021180, 2004.

752 Lelieveld, J., Berresheim, H., Borrmann, S., et al.: Global air pollution crossroads over the
753   Mediterranean, Science, 298, 794–799, 2002.

754 Liu, Y. and Daum, P.: The effect of refractive index on size distributions and light scattering
755   coefficients derived from optical particle counters, J. Aerosol Sci., 31, 945–957, 2000.Loeb, N. G.,
756   and Su, W.: Direct Aerosol Radiative Forcing Uncertainty Based on a Radiative Perturbation
757   Analysis, J. Climate, 23, 5288–5293. doi: http://dx.doi.org/10.1175/2010JCLI3543.1, 2010.

758 Loeb, N. G., and Su, W. Y.: Direct aerosol radiative forcing uncertainty based on a radiative
759   perturbation analysis, J. Clim., 23, 5288–5293, 2010.

760 Lyamani, , H., Olmo, F. J., Alcántara, A., and Alados-Arboledas, L.: Atmospheric aerosols during the
761   2003 heat wave in southeastern Spain. I: Spectral optical depth, Atmos. Environ., 40, 6453–6464,
762   2006.

763 Lyamani, H., Valenzuela, A., Perez-Ramirez, D., Toledano, C., Granados-Muñoz, M. J., Olmo, F. J.,
764   and Alados-Arboledas, L.: Aerosol properties over the western Mediterranean basin: temporal and
765   spatial variability, Atmos. Chem. Phys., 15, 2473-2486, doi:10.5194/acp-15-2473-2015, 2015

766 Mallet, M., Roger, J. C., Despiau, S., Dubovik, O., and Putaud, J. P.: Microphysical and optical
767   properties of aerosol particles in urban zone during ESCOMPTE, Atmos. Res., 69, 73–97, 15
768   2003.

769 Mallet, M., Van Dingenen, R., Roger, J. C., Despiau, S., and Cachier, H.: In situ airborne
770   measurements of aerosol optical properties during photochemical pollution events, J. Geophys.
771   Res., 110, D03205, doi:10.1029/2004JD005139, 2005.

772 Mallet, M., Gomes, L., Solmon, F., Sellegri, K., Pont, V., Roger, J. C., Missamou, T., and Piazzola, J.:
773   Calculation of key optical properties of the main anthropogenic aerosols over the Western French
774   coastal Mediterranean Sea, Atmos. Res., 101, 396–411, 2011.

775   Mallet, M., Dubovik, O., Nabat, P., Dulac, F., Kahn, R., Sciare, J., Paronis, D., and Léon, J. F.:
776   Absorption properties of Mediterranean aerosols obtained from multi-year ground-based remote
777   sensing observations, Atmos. Chem. Phys., 13, 9195-9210, doi:10.5194/acp-13-9195-2013, 2013.

778   McComiskey, A., Schwartz, S. E., Schmid, B., Guan, H., Lewis, E. R., Ricchiazzi, P., and Ogren,
779   J. A.: Direct aerosol forcing: Calculation from observables and sensitivities to inputs, J.
780   Geophys. Res., 113, D09202, doi:10.1029/2007JD009170, 2008.

781   Meloni, D., di Sarra, A., Pace, G., and Monteleone, F.: Aerosol optical properties at Lampedusa
782   (Central Mediterranean). 2. Determination of single scattering albedo at two wavelengths for
783   different aerosol types, Atmos. Chem. Phys., 6, 715-727, doi:10.5194/acp-6-715-2006, 2006.

784   Millán, M. M., Mantilla, E., Salvador, R., Carratala, A., Sanz, M. J., Alonso, L., Gangoiti, G., and
785   Navazo, M.: Ozone cycles in the western Mediterranean basin: interpretation of monitoring data in
786   complex terrain, J. Appl. Meteorol., 4, 487–507, 2000.

787   Müller, D., Ansmann, A., Wagner, F., Franke, K., and Althausen, D.: European pollution outbreaks
788   during ACE 2: Microphysical particle properties and single-scattering albedo inferred from
789   multiwavelength lidar observations, J. Geophys. Res., 107, D15, 4248, 10.1029/2001JD001110,
790   2002.

791   Nabat, P., Somot, S., Mallet, M., Sevault, F., Chiacchio, M. and Wild, M.: Direct and semi-direct
792   aerosol radiative effect on the Mediterranean climate variability using a coupled Regional Climate
793   System Model Clim. Dyn., 44, 1127-1155, doi:10.1007/s00382-014-2205-6, 2015.

794   Nedélec, P., Cammas, J.-P., Thouret, V., Athier, G., Cousin, J.-M., Legrand, C., Abonnel, C.,
795   Lecoeur, F., Cayez, G., and Marizy, C.: An improved infrared carbon monoxide analyser for
796   routine measurements aboard commercial Airbus aircraft: technical validation and first scientific
797   results of the MOZAIC III programme, Atmos. Chem. Phys., 3, 1551–1564, doi:10.5194/acp-3-
798   1551-2003, 2003.

799   Pace, G., di Sarra, A., Meloni, D., Piacentino, S., Chamard, P.: Aerosol optical properties at
800   Lampedusa (Central Mediterranean). 1. Influence of transport and identification of different
801   aerosol types, Atmos. Chem. Phys., 6, 697–713, 2006.

802   Pandolfi, M., Cusack, M., Alastuey, A., and Querol, X.: Variability of aerosol optical properties in the
803   Western Mediterranean Basin Atmos. Chem. Phys., 11, 8189–8203, 2011.

804   Pandolfi, M., et al.: Effects of sources and meteorology on particulate matter in the Western
805   Mediterranean Basin: An overview of the DAURE campaign, J. Geophys. Res. Atmos., 119,
806   4978–5010, doi:10.1002/2013JD021079, 2014.

807   Pérez, N., Pey, J., Castillo, S., Viana, M., Alastuey, A., and Querol, X.: Interpretation of the
808   variability of levels of regional background aerosols in the Western Mediterranean, Sci. Tot.
809   Environ., 407, 527–540, 2008.

810   Pey, J., Querol, X., and Alastuey, A.: Discriminating the regional and urban contributions in the
811   North-Western Mediterranean: PM levels and composition, Atmos Environ, 44, 1587–96, 2010.

812   Piazzola, J., Sellegri, K., Bourcier, L., Mallet, M., Tedeschi, G., and Missamou, T.: Physicochemical
813   characteristics of aerosols measured in the spring time in the Mediterranean coastal zone, Atmos.
814   Environ., 54, 545-556, 2012.

815   Ramana, M. V., and Ramanathan, V.: Abrupt transition from natural to anthropogenic aerosol
816   radiative forcing: Observation at the ABCMaldives Climate Observatory, J. Geophys. Res., 111,
817   D20207, doi:10.1029/2006JD007063, 2006.

818   Raut, J.-C., and Chazette, P.: Vertical profiles of urban aerosol complex refractive index in the frame
819   of ESQUIF airborne measurements, Atmos. Chem. Phys., 8, 901–919, 2008.Russell, P. B.,
820   Bergstrom, R. W., Shinozuka, Y., Clarke, A. D., DeCarlo, P. F., Jimenez, J. L., Livingston, J. M.,
821   Redemann, J., Dubovik, O., and Strawa, A.: Absorption Angstrom Exponent in AERONET and

822   related data as an indicator of aerosol composition, Atmos. Chem. Phys., 10, 1155–1169,
823   doi:10.5194/acp-10-1155-2010, 2010.

824 Saha, A., Mallet, M., Roger, J. C., Dubuisson, P., Piazzola, J., and Despiau, S.: One year
825   measurements of aerosol optical properties over an urban coastal site: Effect on local direct
826   radiative forcing, Atmos. Res., *90*, 195-202, 2008.

827 Stamnes K., Tsay, S. C., Wiscombe, W., and Jayaweera, K.: Numerically stable algorithm for
828   discrete-ordinate-method radiative transfer in multiple scattering and emitting layered media,
829   Appl. Opt., 27, 2502–2509, 1988.

830 Stier, P., Schutgens, N. A. J., Bellouin, N., Bian, H., Boucher, O., Chin, M., Ghan, S., Huneeus, N.,
831   Kinne, S., Lin, G., Ma, X., Myhre, G., Penner, J. E., Randles, C. A., Samset, B., Schulz, M.,
832   Takemura, T., Yu, F., Yu, H., and Zhou, C.: Host model uncertainties in aerosol radiative forcing
833   estimates: results from the AeroCom Prescribed intercomparison study, Atmos. Chem. Phys., 13,
834   3245-3270, doi:10.5194/acp-13-3245-2013, 2013.

835 Stohl, A., Hittenberger, M., and Wotawa, G.: Validation of the Lagrangian particle dispersion model
836   Flexpart against large-scale tracer experiment data, Atmos. Environ., 32, 4245–4264, 1998.

837 Weingartner, E., Saathof, H., Schnaiter, M., Streit, N., Bitnar, B., and Baltensperger, U.: Absorption
838   of light by soot particles: Determination of the absorption coefficient by means of Aethalometers,
839   J. Aerosol Sci., 34, 1445–1463, 2003.

840

841

842

843

844

845

846

847

848

849

850

851

852

853

854

855

856

857

858

859

860

861

862

863 **Tables**

864

865 **Table 1.** Summary of information on the SLRs analysed in this study. The SLR location

866 (within the boundary layer or in the free troposphere) has been determined based on the

867 boundary layer top height estimated for the closest vertical sounding performed during each

868 flight (see Di Biagio et al., 2015). The Sector of origin for sampled air masses has been

869 determined based on FLEXPART back-trajectories.

870

Flight number	SLR_ID	Date	Time start-stop	Altitude (m)	Location	Sector of origin
V19	V19_R1	26/06/2012	11:23-11:38	322	Within the boundary layer	Eastern
V19	V19_R2	26/06/2012	11:44-11:59	897	Within the boundary layer	Eastern
V21	V21_R1	27/06/2012	10:54-11:12	312	Within the boundary layer	Eastern
V21	V21_R2	27/06/2012	11:48-12:04	629	Within the boundary layer	Eastern
V21	V21_R3	27/06/2012	12:05-12:19	311	Within the boundary layer	Western
V22	V22_R1	29/06/2012	7:42-8:01	478	Within the boundary layer	Eastern
V23	V23_R2	29/06/2012	12:05-12:20	319	Within the boundary layer	Open Sea
V25	V25_R1	04/07/2012	9:08-9:24	639	Within the boundary layer	Western
V25	V25_R2	04/07/2012	9:32-9:48	2015	Free troposphere	Western
V25	V25_R3	04/07/2012	9:50-10:08	2538	Free troposphere	Western
V26	V26_R2	04/07/2012	17:08-17:25	1877	Free troposphere	Western
V27	V27_R1	06/07/2012	9:28-9:47	164	Within the boundary layer	Open Sea
V28	V28_R2	06/07/2012	15:58-16:13	927	Within the boundary layer	Open Sea
V30	V30_R1	07/07/2012	14:09-14:28	3498	Free troposphere	Western
V30	V30_R2	07/07/2012	14:51-15:07	549	Within the boundary layer	Open Sea
V31	V31_R1	10/07/2012	15:44-16:20	322	Within the boundary layer	Western
V31	V31_R2	10/07/2012	16:31-16:59	954	Within the boundary layer	Western
V32	V32_R1	11/07/2012	12:52-13:13	250	Within the boundary layer	Western
V32	V32_R2	11/07/2012	13:22-13:48	788	Within the boundary layer	Western
V32	V32_R3	11/07/2012	14:02-14:12	336	Within the boundary layer	Western
V32	V32_R4	11/07/2012	14:18-14:35	802	Within the boundary layer	Western

871

872

Table 2. Summary of the aerosol in situ measurements on the ATR-42 during the TRAQA campaign. Details on the data treatment and uncertainty estimation for the different instruments are provided in Sect. 2.

Property measured	Instrument	Location on aircraft	Flow rate (l min⁻¹)	Time resolution	Size range	Sensitivity or uncertainty	Comments
Aerosol number concentration	Condensation Particle Counter (CPC 3775)	in the cabin behind AVIRAD inlet	1.5	5 sec	0.004 – 3 μm	±10% (concentration)	
Aerosol size distribution	Passive cavity aerosol spectrometer probe (PCASP 100x)	aircraft fuselage, left side before the wing	0.06	1 sec	Nominally 0.1 – 3.0 μm Corrected for refractive index 0.10 – 4.47 μm	<±25% (diameter optical to geometric conversion) ±15% (concentration) (e.g., Highwood et al., 2012)	Aerosol concentration underestimated by 50% between 0.4 and 1.0 μm
	SkyGRIMM 1.129	in the cabin behind AVIRAD inlet	1.3	6 sec	Nominally 0.3 – 32 μm Corrected for refractive index 0.28 – 65.80 μm (AVIRAD 50% cut-off efficiency at ~12 μm diameter)	<±25% (diameter optical to geometric conversion) ±10% (concentration)	Data not available >350 m
Dry aerosol scattering coefficient σ$_s$ (450, 550, 700 nm)	TSI 3563 integrating nephelometer	in the cabin behind AVIRAD inlet	30	6 sec	50% cut-off efficiency at ~12 μm diameter	<±10% for σ$_s$ at 450, 550, and 700 nm	
Aerosol absorption coefficient (σ$_a$) (370, 470, 520, 590, 660, 880, 950 nm)	Magee AE31 aethalometer	in the cabin behind AVIRAD inlet	13	2 min	50% cut-off efficiency at ~12 μm diameter	11-70% variable at the different wavelengths	Data available only for 60% of SLRs

885 **Table 3.** Lognormal mode parameters of the measured aerosol size distribution (total aerosol number concentration, N_{tot}, median diameter, D_g, and geometric standard deviation, σ_g). Data corresponds to SLRs below ~350 m altitude. Diameters are given in microns and number concentrations refer to ambient conditions.

		Mode 1	Mode 2	Mode 3	Mode 4	Mode 5	Mode 6	Mode 7
V19_R1	N_{tot}	498.00	160.00	20.00	4.50	1.95	0.10	
	D_g	0.13	0.24	0.38	0.66	1.55	4.85	
	σ_g	1.19	1.16	1.17	1.29	1.60	1.38	
V21_R1	N_{tot}	600.00	210.00	29.00	5.50	0.55		
	D_g	0.13	0.24	0.37	0.52	1.56		
	σ_g	1.20	1.17	1.15	1.40	1.62		
V21_R3	N_{tot}	600.00	195.00	30.00	2.80	0.48	0.02	
	D_g	0.13	0.23	0.37	0.57	1.55	4.95	
	σ_g	1.19	1.16	1.18	1.33	1.66	1.41	
V23_R2	N_{tot}	660.00	195.00	25.00	3.20	0.75	0.03	
	D_g	0.13	0.23	0.37	0.57	1.59	5.69	
	σ_g	1.19	1.16	1.16	1.37	1.69	1.33	
V27_R1	N_{tot}	930.00	264.00	40.00	4.60	0.52	0.04	0.004
	D_g	0.13	0.23	0.37	0.55	1.57	3.85	8.20
	σ_g	1.19	1.17	1.18	1.38	1.68	1.12	1.26
V31_R1	N_{tot}	482.00	278.00	48.00	2.70	0.55	0.01	
	D_g	0.14	0.24	0.35	0.54	1.82	7.14	
	σ_g	1.20	1.16	1.17	1.39	1.65	1.17	
V32_R1	N_{tot}	1135.00	413.00	55.00	5.00	0.65	0.01	
	D_g	0.13	0.23	0.37	0.50	1.65	7.30	
	σ_g	1.19	1.18	1.16	1.37	1.66	1.11	
V32_R3	N_{tot}	235.00	84.00	12.00	1.80	0.12	0.02	0.004
	D_g	0.14	0.23	0.38	0.50	1.57	3.75	7.99
	σ_g	1.19	1.16	1.16	1.32	1.68	1.12	1.31

889 **Table 4.** Maximum, mean, and minimum of the single scattering albedo considered for radiative transfer calculations. Values are reported at the 7 wavelengths used as inputs in the GAME model.

	330 nm	400 nm	550 nm	670 nm	870 nm	1020 nm	1500 nm
SSA max	0.98	0.98	0.99	0.99	1.00	0.99	0.99
SSA mean	0.93	0.93	0.92	0.91	0.90	0.90	0.89
SSA min	0.88	0.87	0.85	0.85	0.83	0.82	0.80

895 **Figures**

896

897 **Figure 1.** Upper panel: geographical position of the different straight levelled runs (SLRs)

898 performed during the TRAQA campaign and analysed in this paper. The label for each point in the

899 figure identifies the flight number and the corresponding SLR: for example V22_R1 indicates the

900 coordinates of the first SLR of flight V22. Lower panel: definition of three different source areas for

901 the various SLRs (see Sect. 3.1 for more details). The Western sector includes trajectories coming

902 from the Atlantic Ocean and travelling over France or northern Spain before reaching the Western

903 basin; the Eastern sector includes air mass trajectories from continental Europe that have travelled

904 over northern Italy-Po Valley before entering the basin; and the Open Sea sector consists of

905 trajectories which have experienced at least 2 days of subsidence over the sea in the Western basin.

906
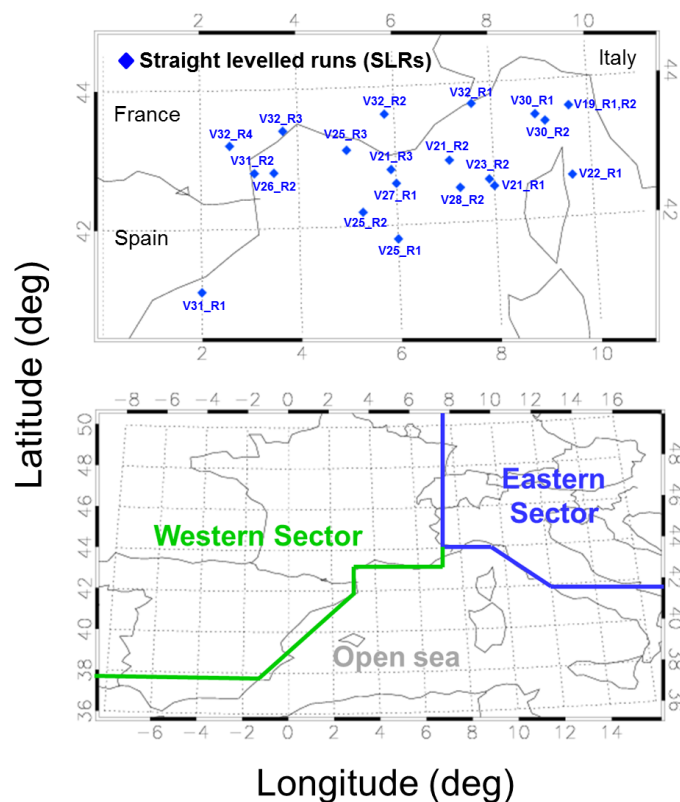
907
908
909

910 **Figure 2.** Averages over the different TRAQA straight levelled runs (SLRs) of the measured:
911 altitude, spectral scattering coefficient (σ_s; 450, 550, and 700 nm), scattering Ångström exponent
912 (SAE), spectral absorption coefficient (σ_{abs}; 370, 470, 520, 590, 660, 880, and 950 nm), absorption
913 Ångström exponent (AAE), ozone enhancement factor ($\Delta O_3/\Delta CO$) and Aitken-to-accumulation
914 ratio (dN_{Aitken}/dN_{Acc}). Uncertainties indicate the 1-σ standard deviation. The x-axis indicates the
915 flight number (19 to 32 for flights V019 to V032); each point for the same flight number represents
916 a different SLR.

917

918
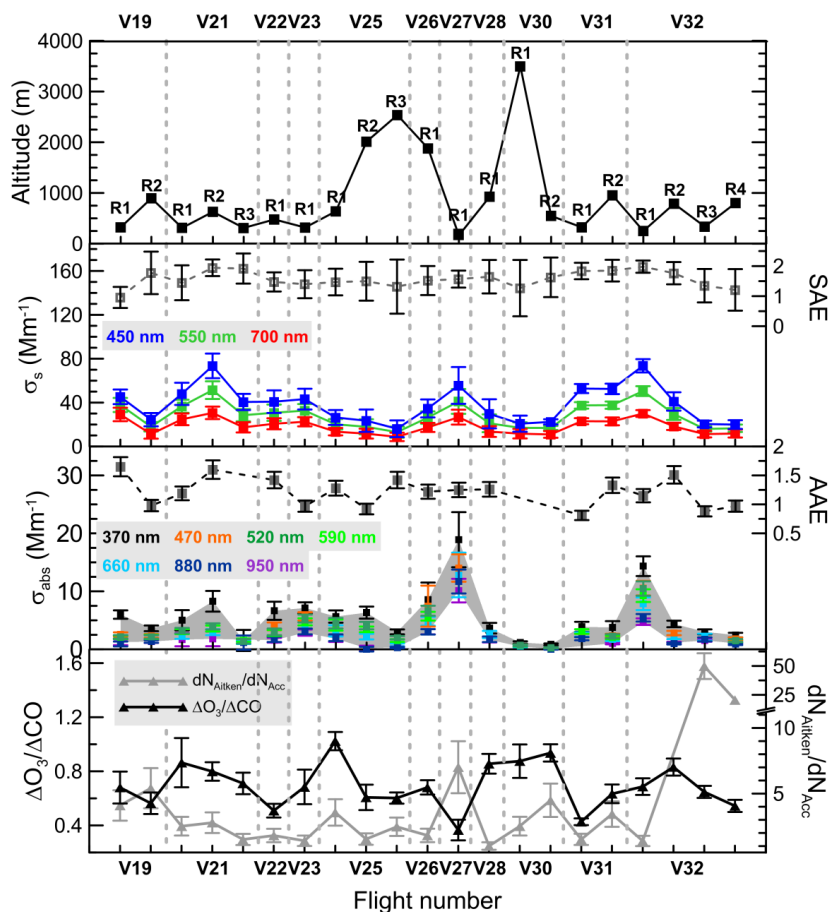
919
920
921

922

923

924   **Figure 3.** Number size distributions (left panel) and volume size distributions (right panel)

925   measured over the different SLRs for the TRAQA flights. Data corresponds to measurements

926   performed within the boundary layer at altitudes <350 m (V19_R1, V21_R1, V21_R3, V23_R2,

927   V27_R1, V31_R1, V32_R1, V32_R3). Concentrations are given at ambient conditions. Grey

928   shading represents minimum and maximum measured values, while the black curve is the average

929   size. Measurement uncertainties are also reported for the average curve.

930
931
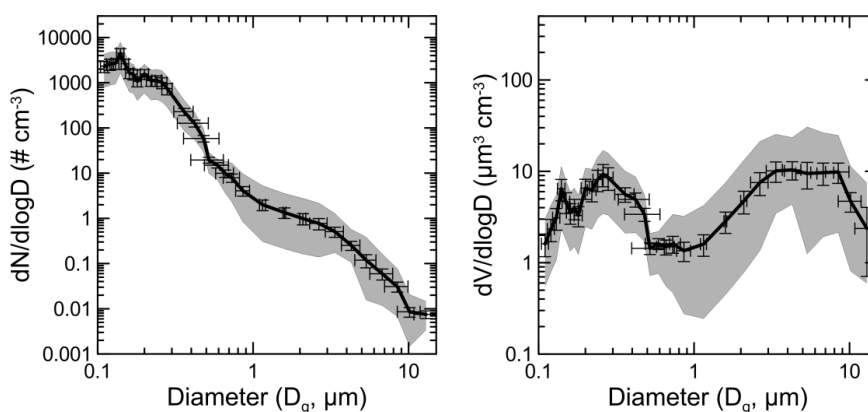
932
933

934   **Figure 4.** Spectral single scattering albedo at seven wavelengths between 370 and 950 nm

935   calculated from nephelometer and aethalometer measurements for the different SLRs within

936   pollution layers. Data are separated based on the different air mass origin (Western Sector, Eastern

937   Sector, and Open Sea).

938

939
940
941
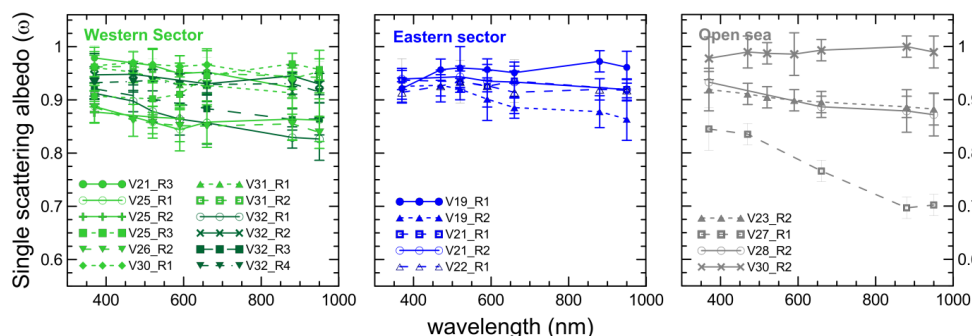
Figure 5. Single scattering albedo (370, 660, and 950 nm), ozone enhancement factor ($\Delta O_3/\Delta CO$),
Aitken-to-accumulation ratio (dN_{Aitken}/dN_{Acc}), and scattering (SAE) and absorption Ångström
exponent (AAE) versus height for all analysed SLRs cases.
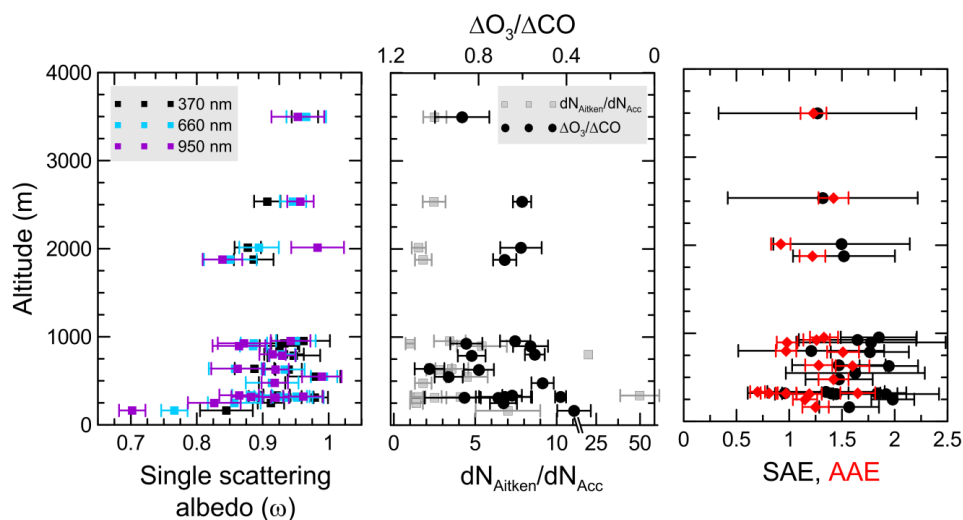
Figure 6. Comparison of the aerosol scattering (σ_s, left panel) and absorption (σ_{abs}, right panel)
coefficients measured by the nephelometer and the aethalometer and calculated from measured size
distribution data with Mie theory. Data are given at ambient conditions.
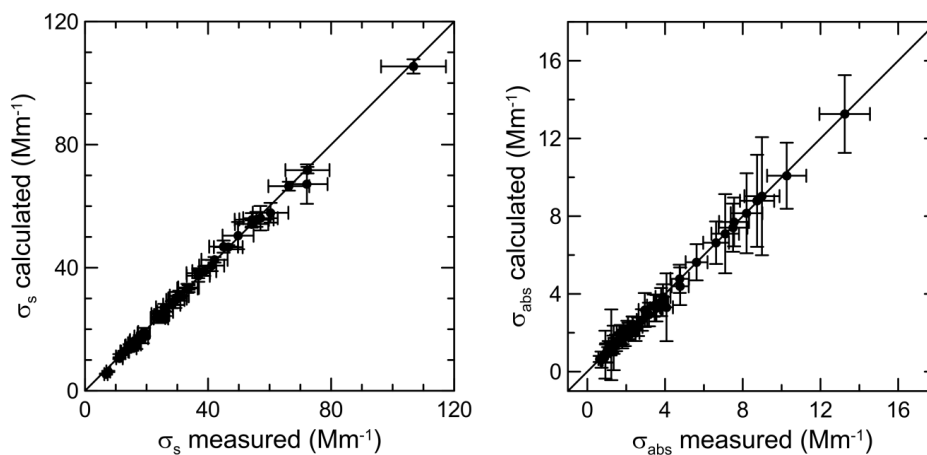
955 **Figure 7.** Spectral real (n, left panel) and imaginary (k, right panel) parts of the complex refractive

956 index obtained by optical closure for the 8 selected case studies. For sake of clarity, uncertainties on

957 n and k are not reported in the plot. The values of the single scattering albedo measured at 370 and

958 950 nm for the different cases are reported in the legend. The spectral real and imaginary parts of

959 the complex refractive index as obtained from the Optical Properties of Aerosols and Clouds

960 (OPAC, Hess et al., 1998) database for insoluble, water soluble, soot and sea salt components are

961 also reported in the plot. These components are used in OPAC to model continental polluted,

962 continental rural, urban, and maritime polluted aerosols.

963
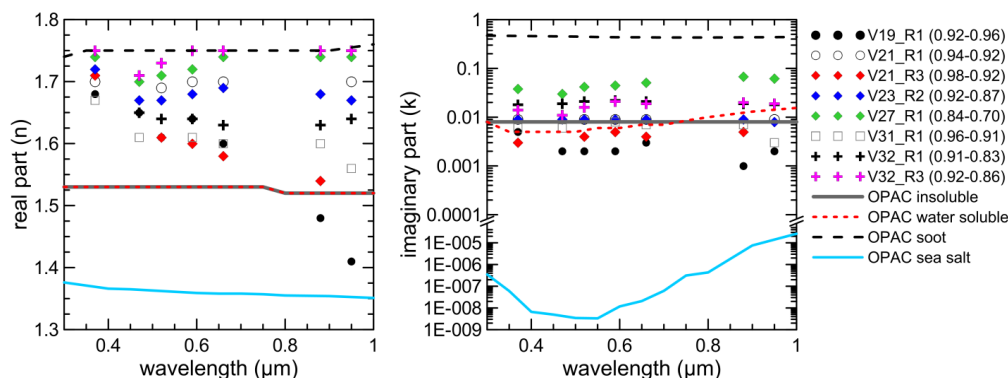
964

965

966 **Figure 8.** Spectral single scattering albedo plotted against the real (left panel) and the imaginary

967 (right panel) parts of the complex refractive index.

968
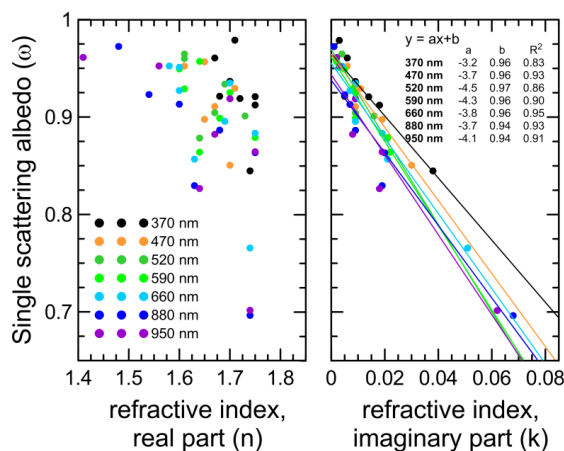
969

970   **Figure 9.** Aerosol shortwave forcing efficiency at 60° solar zenith angle calculated at the surface,

971   TOA, and within the atmosphere for the maximum, mean, and minimum of the single scattering

972   albedo (ω) observed in this study (Table 4).

973

974